[a]Institute of Applied Bioresource Research, College of Animal Sciences, Zhejiang University, Room C319, Agriculture Life and Environmental Sciences Building, 866 Yuhangtang Road, Hangzhou 310058, P. R. China. E-mail: ljzhu@zju.edu.cn; Fax: +86 571 88982185; Tel: +86 571 88982185

[b]Science for Life Laboratory, Division of Polymer Chemistry, Department of Chemistry-Ångström, Uppsala University, Uppsala SE 751 21, Sweden

† Electronic supplementary information (ESI) available: The thermogravimetric analysis results. See DOI: 10.1039/c6ra17199k

gained a lot of attention recently.[28,29] Due to their water insolubility, mSF can be uniformly disper matrixes to fabricate mSF-reinforced bioco example, the Kaplan group added mSF into silk silk hydrogels,[31] respectively, and the obtai showed a significant improvement in their mec mance. We used mSF to prepare an mSF/chi membrane[32] in which the mSF also acted

a reinforced phase to enhance the elastic modulus for dozens of times. Moreover, these fine-scale mSF displayed good biological efficiency both *in vitro* and *in vivo*.[30–32] Nevertheless, there are almost no reports describing the fabrication of mSF/HAp materials, which may have predictable application as injectable bone defect fillers or as a mechanical reinforcement in bone tissue-engineered scaffolds.

In the current study, we have prepared relatively homogenous mSF in lengths of 200–300 μm *via* alkali-hydrolysis and milling-selection methods, and then used them as templates for biomineralization. Bone-like HAp apatites can be spontaneously formed in a hierarchical fashion on the surface of the mSF with good interface combination between the organic and inorganic phases, and the mSF/HAp biocomposites achieved better cellular outcomes.

## 2. Results and discussion

### 2.1 The morphology of silk microfibers (mSF) and minerali ed silk microfibers (mmSF)

A two-step method using alkali-hydrolysis and milling-selection was comprehensively applied to prepare the mSF used in this study. From visual inspection the mSF was a fine white powder and from microscopic observations they were in a fiber form (Fig. 1). The diameter of the mSF was about 10 μm and the length was kept homogenous within 200–300 μm (Fig. 1b) because the long silk fibers had been chopped into short fibers under the alkaline conditions and the tiny silk particles were successfully removed using a sieve. The surface of the mSF was relatively smooth with hardly any attachment (Fig. 1c), mainly due to the total degumming of sericin.

The biomineralization of the mSF was carried out in 1.5 × SBF, an effective biomimetic mineralizing solution,[33,34] which provides an *in situ* mineral deposition environment. Although nothing significantly changed in the mSF after immersion in the 1.5 × SBF for 1 d (Fig. 2a), two days later emerged many spherical and near-spherical crystals onto the mSF surface, isolated or connected (Fig. 2b). The microstructure in vertical and lateral views of representative mineral crystals are shown in Fig. 2e and f. Actually these flower-like microspheres with diameters of around 1 μm presented sophisticated structures, which were comprised of many nanosized plate-like crystals in various orientations. As basic building blocks, nanoplates can self-assemble into different morphologies and architectures, which provide an efficient "bottom-up" route to fabricate bone-like hierarchical materials.[7,35]

Upon increasing the mineralization time, a growing number of crystals were continually formed and they tended to aggregate together, thus developing into a hierarchical mineral layer. After immersion in 1.5 × SBF for 5 d, the layer was not very complete as some intervals still existed (Fig. 2c). When it came to 7 d, the mSF had been overcovered (Fig. 2d) and the surface of the mineral layer was fairly rough, which was attributed to the nanoplates confluence (Fig. 2g). The time-dependent manner of mineral deposition was also reflected in the thermogravimetric analysis shown in Fig. S1 (see the ESI).† All the samples showed mass-loss behavior as the temperature was increased, while at the end the remaining weight percentage of the mmSF increased with prolonged mineralization time.

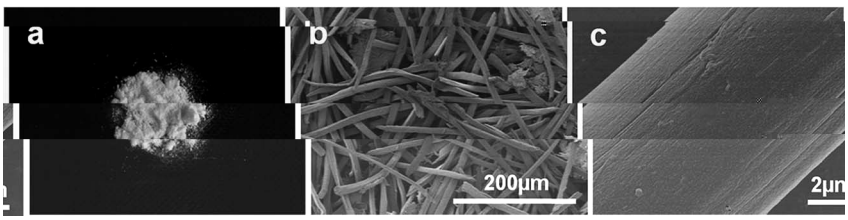


Fig. 1 (a) A digital image of the mSF. (b) FE-SEM images of the mSF at low magnification and (c) high magnification.

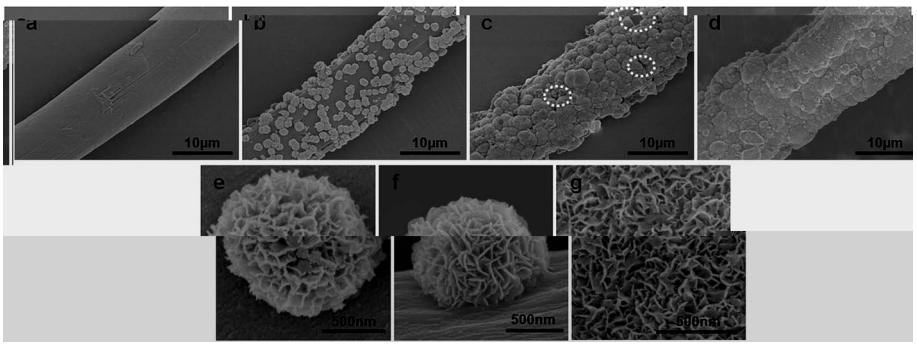


Fig. 2 FE-SEM images of the mmSF after mineralization in 1.5 × SBF for 1 d (a), 3 d (b), 5 d (c) (the white dotted boxes indicate the uncovered areas) and 7 d (d). Vertical (e) and lateral (f) views of a single spherical flower-like mineral crystal. (g) The surface morphology of confluent mineral layer.

### 2.2 Characteri ation and analysis of the deposited mineral

To visually demonstrate the elemental spatial distribution of the deposited minerals, EDX elemental analysis in area scan mode was performed. Three elements (oxygen, phosphorus and calcium) were detected in the mineral layer of the mmSF (Fig. 3A) and they distributed in the whole area at a very high density, indicating the mineral was a type of calcium phosphate. Also, the mapping result in Fig. 3B clearly shows that these elements were mainly concentrated in areas consistent with the shape of the single crystals on the mSF, especially calcium.

XRD measurements were used to further analyze the crystallographic properties of the mSF and mmSF for various mineralization periods. Pure HAp was selected as reference with all the characteristic diffraction peaks designated in accordance with the standard card (JCPDS 09-0432) (Fig. 4Af). The broad peak at 20.7° (Fig. 4Aa) was attributed to the β-sheet crystalline domain of the mSF,[36] as the inner well-ordered structure still existed. No significant changes happened after mineralization for 1 d, but two intense peaks at 31.73° and 45.47° corresponding to the (211) and (222) lattice planes emerged on the 3rd day, which was due to the formation of spherical mineral crystals that were detectable by XRD. Upon increasing the mineralization time from 3 d to 5 d and 7 d, one interesting phenomenon was that the (222) lattice plane disappeared, while the peak at 25.93° corresponding to the (002) lattice plane clearly appeared and gradually strengthened, suggesting the lattice plane transformed during the confluence process from independent crystals to a connected mineral layer. In addition, the peak observed for the (211) lattice plane broadened and tended to divide into multiple peaks, which was a result of the decreased crystallinity.[37]

FTIR spectroscopy was applied to identify the functional groups and analyze the molecular structure of the mmSF using the mSF as a reference (Fig. 4B). Amide I (C=O stretching), amide II (N–H deformation and C–N stretching) and amide III (C–N stretching and N–H deformation) are the characteristic peaks observed for silk fibroin and appeared at 1645 $cm^{-1}$, 1516 $cm^{-1}$ and 1230 $cm^{-1}$, respectively in curve a. Amide I shifted to a lower wavenumber at ~1630 $cm^{-1}$ after mineralization, indicating an interaction had occurred between $Ca^{2+}$ and $COO^{-}$.[38] Although no mineral deposition was observed on the mSF at day 1 according to SEM images, the $Ca^{2+}$ in 1.5 × SBF can bond with $COO^{-}$ to promote the initial nucleation step. The mineral crystals grew to certain sizes after mineralization for 3 days, but the relevant curve c had no significant change because the mineral deposition was small during this period. Nevertheless, a series of peaks emerged after mineralization for 5 and 7 d. The intense peaks at 567 $cm^{-1}$ and 603 $cm^{-1}$ were attributed to the O–P–O bending vibrations and the peaks at 962 $cm^{-1}$ and 1035 $cm^{-1}$ were assigned to the P–O stretching vibrations of the phosphate groups.[39] The peak at 873 $cm^{-1}$ and the weak peak at 1415 $cm^{-1}$ should be induced by the absorption bands of the $CO_3^{2-}$ groups,[11,40] which probably come from the atmosphere during the stirring process. It is the $CO_3^{2-}$ incorporation that leads to the decreased crystallinity as the peak for the (211) lattice plane broadened in the XRD pattern.

Based on above results and analyses, we concluded that the deposited minerals was comprised of a carbonate apatite similar to natural bone minerals.[3]

### 2.3 The interface between the minerals and mSF

In order to deeply understand the interface between the inorganic minerals and organic mSF, the cross-sections of the mmSF at 7 d were used for TEM observations. A clear interface can be observed in Fig. 5a and c, but unlike the overcover effect of mineral crystals in the SEM image, some dropped out from the mSF surface (shown in the purple dotted box of Fig. 5a), which may be caused by the powerful cutting stress used when preparing the ultrathin sections for TEM. Fig. 5b shows the magnified cross-section of the mineral crystals, which exhibit similar flower-like structures to those observed using SEM shown in Fig. 2e and f. As mentioned previously, the nanoplates self-assembled into sophisticated structures, herein the needle-like crystals (actually the cross-sections of the plate-like crystals) were aggregated with random orientations.

The HR-TEM observations are shown in Fig. 5d–f, from which more detailed information on the crystal properties could

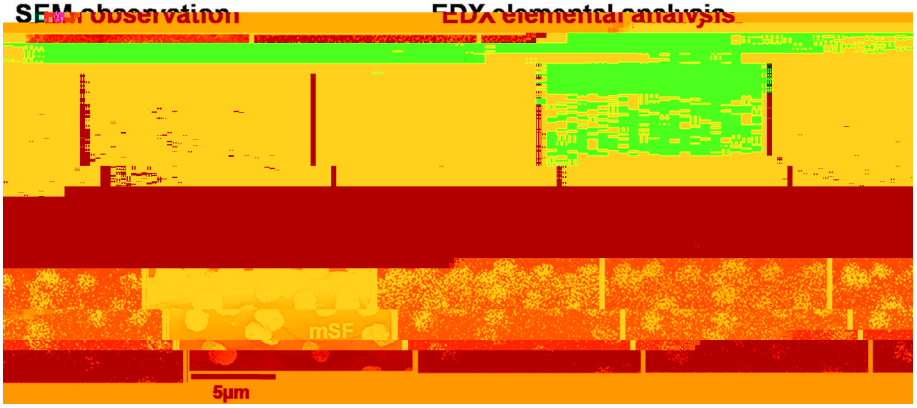


Fig. 3 FE-SEM observations combined with EDX elemental analysis in area scan mode of (A) the mineral layer of the mmSF and (B) the mineral crystals on the mSF (the colors green, purple and blue represent the elements oxygen, phosphorus and calcium, respectively).

 

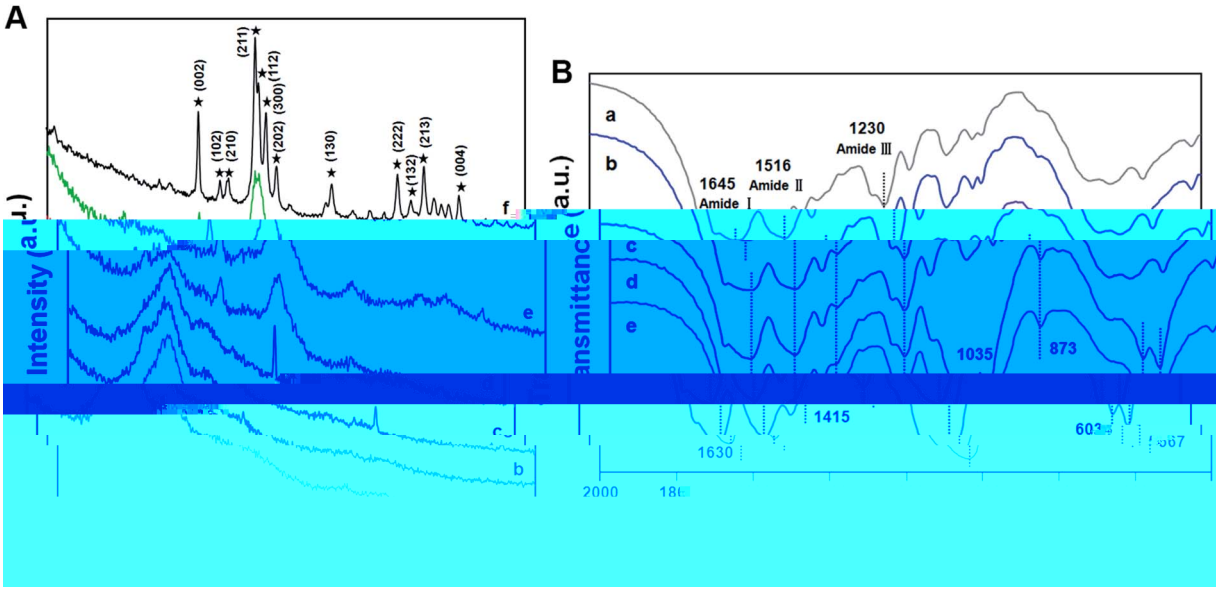


Fig. 4 (A) The XRD spectra of the mSF (a) and mmSF after mineralization in 1.5 × SBF for 1 d (b), 3 d (c), 5 d (d), 7 d (e) and (f) pure HAp. (B) The FT-IR spectra of the mSF (a) and mmSF after mineralization in 1.5 × SBF for 1 d (b), 3 d (c), 5 d (d) and 7 d (e).

be revealed. Two main diffraction rings were detected using the SAED image (Fig. 5e), referring to the (211) and (002) lattice planes. Moreover, Fig. 5f directly shows the lattice images, for the lattice spacings of 0.282 nm and 0.344 nm corresponding to the (211) and (002) lattice planes,[41] which were in accordance with the XRD analysis.

### 2.4 The biomineralization process of the mSF

In the biomineralization process, the organic templates regulate the crystal growth and morphology. Considered as initial nucleation sites, the anionic groups of the templates can chelate calcium ions, arrange the structure and modulate the formation of HAp crystals.[42,43] Unlike materials derived from silk solution in which the anionic groups are adequately exposed, the original silk fibers with insufficient anionic groups probably weaken its $Ca^{2+}$ bonding capability. For example, Takeuchi *et al.*[25] found no apatite could be deposited on degummed long silk fibers after 7 d of mineralization, with or without $CaCl_2$ solution pretreatment. Aiming to provide more active sites to connect with $Ca^{2+}$, Korematsu *et al.*[26,27] modified silk fibers using graft polymerization through

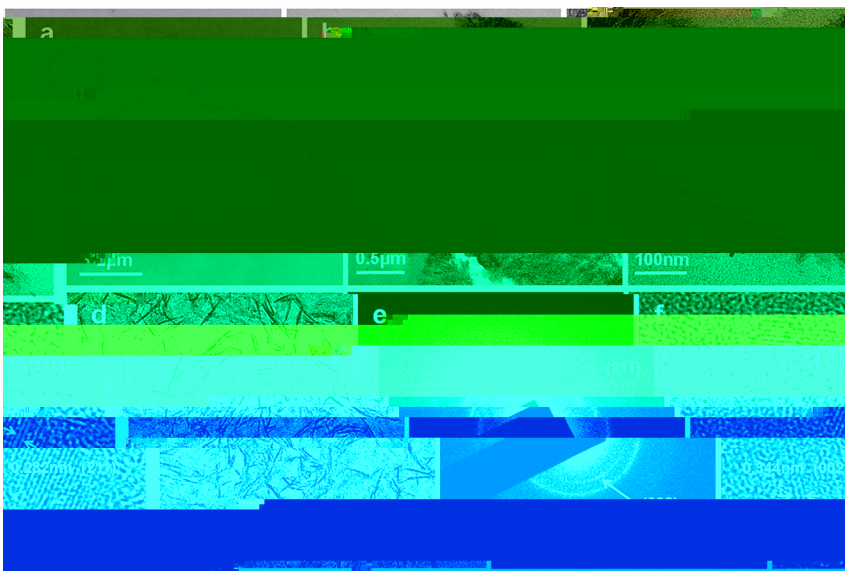


Fig. 5 (a–c) TEM images of the cross-sections of the mmSF after mineralization in 1.5 × SBF for 7 d (the purple dotted lines indicate the interface between the mSF and deposited mineral crystals, and the crystals in purple dotted box were dropped out from the mSF surface). (d, f) HR-TEM images and (e) SAED pattern of the mineral crystals (the diffraction rings were calibrated as the (002) and (211) lattice planes and the lattice spacings of 0.344 nm and 0.282 nm correspond to the *d*-spacings of the (002) and (211) lattice planes, respectively).

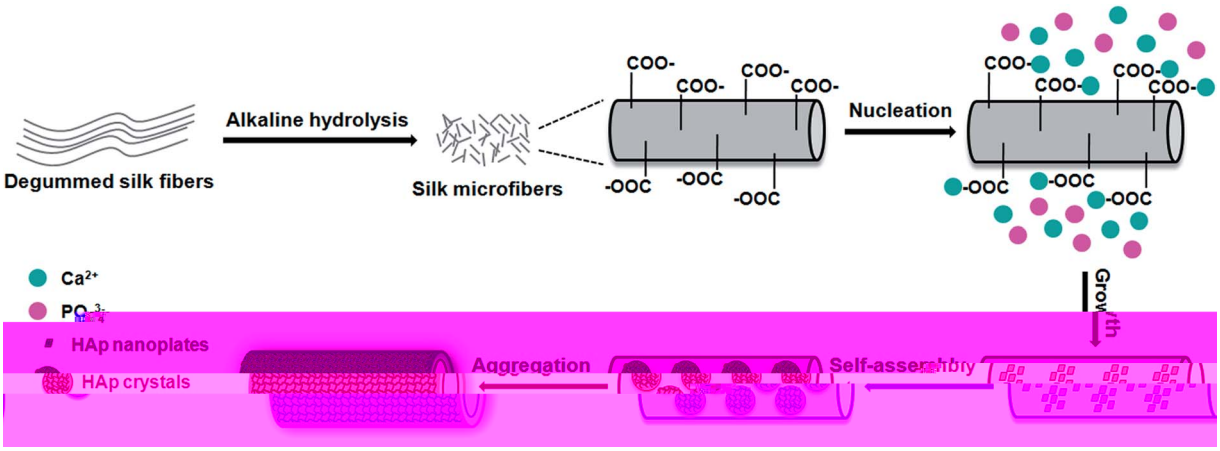


Fig. 6 A schematic representation of the biomineralization process including the nucleation, growth, self-assembly and aggregation of the mSF.

covalent linkages, however, the small amount of mineral deposition indicated it was not a very effective method. However, in our study the mSF can successfully be used as a template to promote the formation of a hierarchical HAp mineral layer. We deduced that these results came from the influence of the alkaline hydrolysis step because the long silk fibers were chopped into relatively short mSF and the surface of the mSF were partly "remodeled" by the $OH^-$ ions, as more $COO^-$ groups were exposed to act as initial $Ca^{2+}$ binding sites.[44,45]

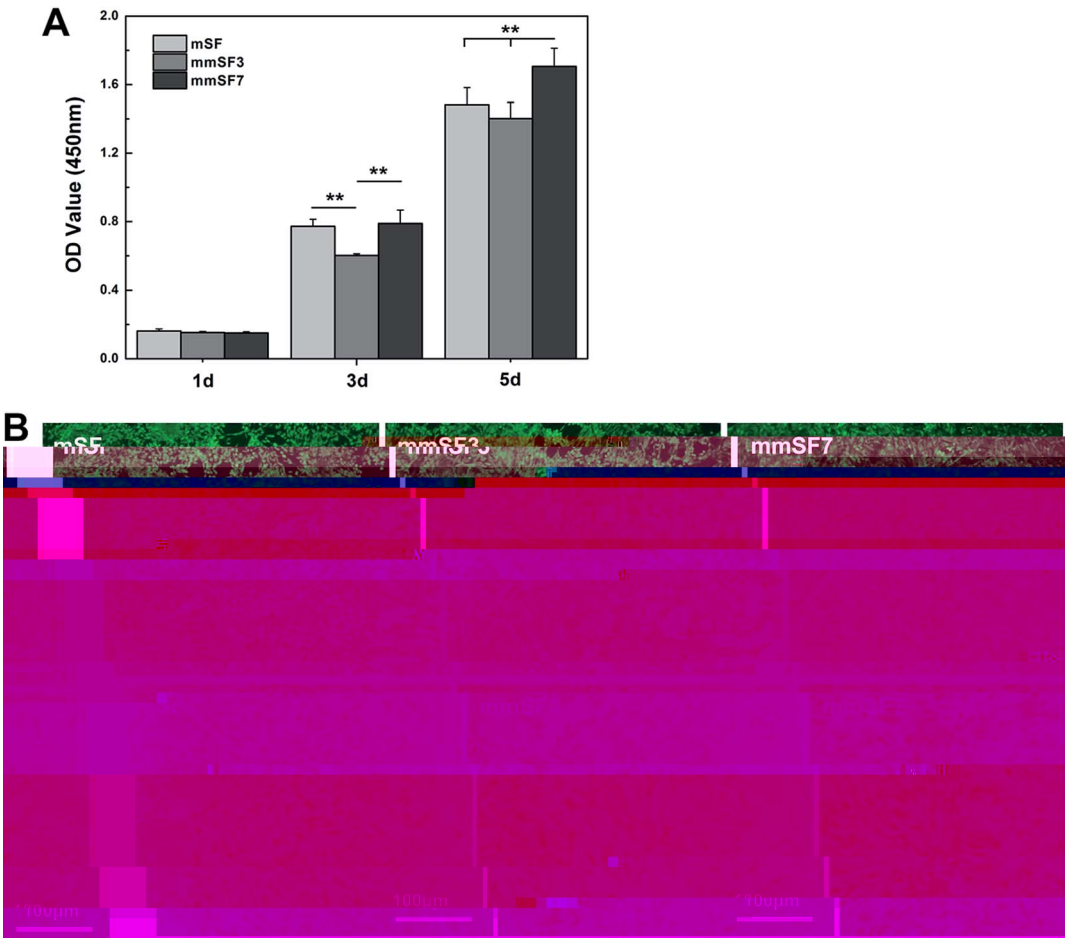


Fig. 7 (A) Proliferation of MG-63 cells after being cultured for different periods of time (1 d, 3 d and 5 d) reflected by the OD value at 450 nm. (B) Calcein-AM staining images of the MG-63 cells after being cultured for 5 d.

 

Based on the previously reported mechanism and our observations in this study, a schematic diagram of HAp formation using the mSF templates was proposed (Fig. 6). The mechanism includes four stages: nucleation, growth, self-assembly and aggregation. In the early stage of mineralization, $Ca^{2+}$ in 1.5 × SBF can bond with the $COO^-$ groups in the mSF to form ion complexes *via* electrostatic interactions. The COO–Ca complexes can then further interact with $PO_4^{3-}$, thus initiating the HAp nucleation stage. When more and more $Ca^{2+}$ and $PO_4^{3-}$ are attracted, HAp nanoplates of a certain size gradually develop. As the basic unit, they will assembly into HAp microspheres exhibiting sophisticated flower-like structures. As mineralization proceeds, the HAp microspheres aggregate into a hierarchical coverage layer, not only achieving a good combination between the organics and inorganics but also generate the novel mSF/HAp biocomposite.

### 2.5 The biocompatibility of the mSF and mmSF

In this study, the biocompatibility of the mSF (silk microfibers without mineralization), mmSF3 (silk microfibers after 3 d of mineralization) and mmSF7 (silk microfibers after 7 d of mineralization) was tested on human osteosarcoma MG-63 cells, which express many characteristics of relatively immature osteoblasts.[46] The viability of the cells at different time points was measured using a CCK-8 kit and the results are shown in Fig. 7. At 1 d, the $OD_{405}$ of three groups were similar, as the addition of materials created a new environment and an adaption period was needed for the cells. At 3 d, significant differences ($p < 0.01$) were observed both between the mmSF3 group and the other groups, respectively. One plausible reason was the incomplete mineral surface of mmSF3 improved the foreign heterogeneity when exposed to cells, while the mSF and mmSF7 were nearly homogeneous. After 5 days of culture, the cells treated with mmSF7 achieved the highest viability and presented significant differences ($p < 0.01$) with the other two groups. The Calcein-AM staining images also supported the CCK-8 assay results. Under low magnification, the cells had overgrown the whole area in the mmSF7 group while not completely in the mSF and mmSF3 groups. Interestingly, no significant difference ($p > 0.05$) was observed between the mSF and mmSF3 groups, for the foreign heterogeneity did not influence the relatively long term proliferation of the MG-63 cells. Under high magnification, the cellular morphology exhibited a more prolonged state when treated with mmSF3 or mmSF7 when compared with the mSF. The improved morphology indicated the cells can sense the surrounding microenvironment and the HAp-containing materials promoted their growth and proliferation. The mSF/HAp biocomposites showed good cytocompatibility, which is important and necessary for further application in bone tissue engineering.

## 3. Experimental section

### 3.1 Materials

Silk cocoons of *Bombyx mori* were provided by the Institute of Huzhou Cocoon Testing (PR China). The 1.5 times simulated body fluid (1.5 × SBF) was prepared according to the components and procedure reported in the literature,[47] which has 1.5 times the ion concentration of SBF. NaCl, $NaHCO_3$, KCl, $K_2HPO_4 \cdot 3H_2O$, $MgCl_2 \cdot 6H_2O$, HCL, $CaCl_2$, $Na_2SO_4$ and Tris, as well as $NaHCO_3$ and NaOH were purchased from Sinopharm Chemical Reagent Co., Ltd. Pure hydroxylapatite (<100 nm) was purchased from Aladdin Industrial Corporation. All reagents were of analytical grade and were used as received without any further purification.

### 3.2 Preparation of the mSF

mSF were obtained using a two-step method, namely alkali-hydrolysis and milling-selection. Firstly, silk cocoons were cut into pieces and degummed twice in 0.5 wt% $Na_2CO_3$ solution at 100 °C, each for 30 min. After thoroughly rinsing and drying, the degummed silk fibers were immersed in 1 M NaOH solution at 40 °C for 5 h. The alkaline hydrolysis was stopped by removing alkaline liquid and washing the degraded product with deionized water. Then, the dried product was bead-milled to further disperse and shortening the silk fibers, and finally the as-prepared mSF was sieved to filter out the ultrashort silk fibers.

### 3.3 Biominerali ation of the mSF

A certain amount of mSF was uniformly dispersed in 1.5 × SBF (1 g : 1000 mL) with magnetically stirring to prevent the mSF from coagulating. The mineralization process was kept at 37 °C and the 1.5 × SBF was changed every day. At a set time of 1, 3, 5 and 7 d, the mineralized silk microfibers (mmSF) were removed and washed with deionized water, then lyophilized using a vacuum freeze dryer (Boyikang, FD-1-50, China).

### 3.4 Characteri ation of the mSF and mmSF

**3.4.1 Field emission scanning electron microscopy (FE-SEM) observations and energy dispersive X-ray spectrum (EDX) elemental analysis.** FE-SEM (SU8010, Hitachi, Japan) with an accelerating voltage of 20 kV was used to observe the morphology and microstructure of the silk microfibers with or without mineralization. The deposited mineral crystals, together with mmSF at certain time points were elemental analyzed using a matched EDX spectrometer (80, Oxford Diffraction, UK) in area scan mode. All the samples were in a dry state and sputtered with gold ions before observation.

**3.4.2 Thermogravimetric analysis (TGA).** A TGA instrument (DTG-60A, Shimadzu, Japan) was used for the thermogravimetric analysis of the mmSF at different time points. The tests were performed under a nitrogen atmosphere (50 mL $min^{-1}$) and the temperature was increased from 50 to 600 °C at a ramp rate of 10 °C $min^{-1}$.

**3.4.3 X-ray powder diffraction (XRD).** The crystallographic properties of the mSF and mmSF at different time points were analyzed using XRD (Empyrean 200895, PANalytical B.V., The Netherlands) equipped with a Cu Kα radiation source ($\lambda$ = 1.5418 Å) in the $2\theta$ range of 20–60°. The step size was 0.02° and the scan rate was 5.0° $min^{-1}$.

**3.4.4 Fourier transform infrared spectroscopy (FTIR).** The mSF and mmSF at different time points were mixed with KBr in

a ratio of 1 : 100 and pressed into tablets. An FTIR spectrometer (8400S, Shimadzu, Japan) was used to record the infrared spectra in the range of 400–4000 $cm^{-1}$. Each spectrum was obtained by the accumulation of 80 scans with a resolution of 4 $cm^{-1}$.

**3.4.5 Transmission electron microscopy (TEM), high-resolution transmission electron microscopy (HR-TEM) and selected area electron diffraction (SAED) analysis.** The ultrathin section samples were made from the cross-sections of the mmSF after 7 d of mineralization using a conventional procedure including fixation, dehydration, embedding, sectioning and staining. Then, the interface between the minerals and silk microfibers was observed by TEM (JEM-1230, JEOL, Japan), HR-TEM (2100F, JEOL, Japan) and SAED, which were used to analyze the crystallographic properties such as the lattice image and lattice plane of the mineral crystals.

### 3.5 Cell proliferation and morphology

Human osteosarcoma MG-63 cells (kindly provided by Prof. Juming Yao from Zhejiang Sci-Tech University and carefully preserved in our laboratory) were employed to evaluate the cytocompatibility of the mSF (silk microfibers without mineralization), mmSF3 (silk microfibers after 3 d of mineralization) and mmSF7 (silk microfibers after 7 d of mineralization). The MG-63 cells were cultured in high-glucose Dulbecco's modified eagle's medium (DMEM) culture medium with 10% fetal bovine serum (FBS, Gibco®, USA), 100 U $mL^{-1}$ penicillin and 100 μg $mL^{-1}$ streptomycin at 37 °C in a humidified air containing 5% $CO_2$. The cells were seeded in 48-well plates with $1 \times 10^4$ cells in each well and cultured for 6 h beforehand, then sterilized samples of the mSF, mmSF3 and mmSF7 were added at a concentration of 1 mg $mL^{-1}$. After being co-cultured for 1, 3 and 5 d (the culture medium was changed every 2 days), the viability of the cells was investigated using a CCK-8 (Cell Counting Kit-8) assay according to the manufacturer's protocol (Biosharp). The optical density values at 450 nm ($OD_{450}$) were detected using a microplate reader (Elx808, Biotek, USA) and the background absorbance of wells containing no cells was subtracted from each group. The results were presented as the mean value ± the standard deviation ($n = 5$) and statistically significant differences (**$p < 0.01$) were determined using one-way ANOVA with *t*-test. In addition, a calcein-AM staining kit (Yeason) was used to further illustrate the proliferation and morphology of the live cells at 5 d of culture. The stained cells were observed under a fluorescence microscope (IX51, Olympus, Japan).

## 4. Conclusions

This study provides a facile method to develop mSF-HAp composites *via* biomineralization. mSF can be used as a template to mediate the formation of hierarchical HAp mineral layer aggregated by flower-like microspheres, which were assembled from nanoplate building blocks. In addition, the organic/inorganic biocomposites exhibited good cytocompatibility. The mSF possess a significant mechanical reinforcement effect and HAp has remarkable osteoinductivity, so we can speculate that the as-prepared materials may achieve good performance in bone tissue engineering. A subsequent study based on this novel biomaterial, such as injectable bone defect fillers or reinforcement in bone repair scaffolds will be further investigated.

## Acknowledgements

This study is supported by the Earmarked Fund (CARS-22-ZJ0402) for China Agriculture Research System (CARS) and the National Natural Science Foundation of China.

## References

1 M. M. Stevens, *Mater. Today*, 2008, **11**, 18–25.
2 J. Henkel, M. A. Woodruff, D. R. Epari, R. Steck, V. Glatt, I. C. Dickinson, P. F. Choong, M. A. Schuetz and D. W. Hutmacher, *Bone Res.*, 2013, **1**, 216–248.
3 S. Weiner and H. D. Wagner, *Annu. Rev. Mater. Res.*, 1998, **28**, 271–298.
4 M. W. Laschke, A. Strohe, M. D. Menger, M. Alini and D. Eglin, *Acta Biomater.*, 2010, **6**, 2020–2027.
5 K. Masanori, *Biol. Pharm. Bull.*, 2013, **36**, 1666–1669.
6 H. Yang, X. Yan, M. Ling, Z. Xiong, C. Ou and W. Lu, *Int. J. Mol. Sci.*, 2015, **16**, 6113–6123.
7 H. Zhou and J. Lee, *Acta Biomater.*, 2011, **7**, 2769–2781.
8 M. Sadat-Shojai, M. T. Khorasani, E. Dinpanah-Khoshdargi and A. Jamshidi, *Acta Biomater.*, 2013, **9**, 7591–7621.
9 M. H. Fathi and A. Hanifi, *Mater. Lett.*, 2007, **61**, 3978–3983.
10 H. B. Zhang, K. C. Zhou, Z. Y. Li and S. P. Huang, *J. Phys. Chem. Solids*, 2009, **70**, 243–248.
11 M. G. Ma, *Int. J. Nanomed.*, 2012, **7**, 1781–1791.
12 W. Y. Zhou, M. Wang, W. L. Cheung, B. C. Guo and D. M. Jia, *J. Mater. Sci.: Mater. Med.*, 2008, **19**, 103–110.
13 K. Lin, X. Liu, J. Chang and Y. Zhu, *Nanoscale*, 2011, **3**, 3052–3055.
14 S. K. Saha, A. Banerjee, S. Banerjee and S. Bose, *Mater. Sci. Eng., C*, 2009, **29**, 2294–2301.
15 Y. Cai and J. Yao, *Nanoscale*, 2010, **2**, 1842–1848.
16 J. Ma, J. Wang, X. Ai and S. Zhang, *Biotechnol. Adv.*, 2014, **32**, 744–760.
17 J. Melke, S. Midha, S. Ghosh, K. Ito and S. Hofmann, *Acta Biomater.*, 2015, **31**, 1–16.
18 F. Mottaghitalab, H. Hosseinkhani, M. A. Shokrgozar, C. Mao, M. Yang and M. Farokhi, *J. Controlled Release*, 2015, **215**, 112–128.
19 B. Kundu, R. Rajkhowa, S. C. Kundu and X. Wang, *Adv. Drug Delivery Rev.*, 2012, **65**, 457–470.
20 N. Kasoju and U. Bora, *Adv. Healthcare Mater.*, 2012, **1**, 393–412.
21 Y. Li, Y. Cai, X. Kong and J. Yao, *Appl. Surf. Sci.*, 2008, **255**, 1681–1685.
22 K. Wei, Y. Li, K. O. Kim, Y. Nakagawa, B. S. Kim, K. Abe, G. Q. Chen and I. S. Kim, *J. Biomed. Mater. Res., Part A*, 2011, **97**, 272–280.

 

23 Y. Jin, B. Kundu, Y. Cai, S. C. Kundu and J. Yao, *Colloids Surf., B*, 2015, **134**, 339–345.
24 C. Holland, A. E. Terry, D. Porter and F. Vollrath, *Polymer*, 2007, **48**, 3388–3392.
25 A. Takeuchi, C. Ohtsuki, T. Miyazaki, H. Tanaka, M. Yamazaki and M. Tanihara, *J. Biomed. Mater. Res., Part A*, 2003, **65**, 283–289.
26 A. Korematsu, T. Furuzono, S. Yasuda, J. Tanaka and A. Kishida, *J. Mater. Sci.: Mater. Med.*, 2004, **39**, 3221–3225.
27 A. Korematsu, T. Furuzono, S. Yasuda, J. Tanaka and A. Kishida, *J. Mater. Sci.: Mater. Med.*, 2005, **16**, 67–71.
28 B. Q. Pei, H. Li, G. Zhu, D. Y. Li, Y. B. Fan and S. Q. Wu, *BioMed Res. Int.*, 2013, **2013**, 945–953.
29 X. Li, Y. Yang, Y. Fan, Q. Feng, F. Z. Cui and F. Watari, *J. Biomed. Mater. Res., Part A*, 2014, **102**, 1580–1594.
30 B. B. Mandal, A. Grinberg, E. S. Gil, B. Panilaitis and D. L. Kaplan, *Proc. Natl. Acad. Sci. U. S. A.*, 2012, **109**, 7699–7704.
31 S. Yodmuang, S. L. McNamara, A. B. Nover, B. B. Mandal, M. Agarwal, T. A. Kelly, P. H. Chao, C. Hung, D. L. Kaplan and G. Vunjak-Novakovic, *Acta Biomater.*, 2014, **11**, 27–36.
32 Z. P. Xu, L. Y. Shi, M. Y. Yang, H. P. Zhang and L. J. Zhu, *J. Mater. Chem. B*, 2015, **3**, 3634–3642.
33 X. Liu, L. A. Smith, J. Hu and P. X. Ma, *Biomaterials*, 2009, **30**, 2252–2258.
34 M. Yang, G. Zhou, Y. Shuai, J. Wang, L. Zhu and C. Mao, *J. Mater. Chem. B*, 2015, **28**, 2455–2462.
35 K. Bleek and A. Taubert, *Acta Biomater.*, 2013, **9**, 6283–6321.
36 U. J. Kim, J. Park, H. J. Kim and D. L. Kaplan, *Biomaterials*, 2005, **26**, 2775–2785.
37 Y. Huang, G. Zhou, L. Zheng, H. Liu, X. Niu and Y. Fan, *Nanoscale*, 2012, **4**, 2484–2490.
38 F. Lin, Y. C. Li, J. Jin, Y. R. Cai, K. M. Wei and J. M. Yao, *Mater. Chem. Phys.*, 2008, **111**, 92–97.
39 X. Y. Zhao, Y. J. Zhu, J. Zhao, B. Q. Lu, F. Chen, C. Qi and J. Wu, *J. Colloid Interface Sci.*, 2014, **416**, 11–18.
40 H. P. Zhang, X. Y. Wang, S. J. Min, M. Mandal, M. Y. Yang and L. J. Zhu, *Ceram. Int.*, 2014, **40**, 985–991.
41 M. Yang, Y. Shuai, C. Zhang, Y. Chen, L. Zhu, C. Mao and H. OuYang, *Biomacromolecules*, 2014, **15**, 1185–1193.
42 J. D. Hartgerink, E. Beniash and S. I. Stupp, *Science*, 2001, **294**, 1684–1688.
43 F. Z. Cui, Y. Wang, Q. Cai and W. Zhang, *J. Mater. Chem.*, 2008, **18**, 3835–3840.
44 L. Wang, C. Li and M. Senna, *J. Nanopart. Res.*, 2007, **9**, 919–929.
45 P. Taddei, E. Pavoni and M. Tsukada, *J. Raman Spectrosc.*, 2016, **47**, 731–739.
46 C. C. Ribeiro, C. C. Barrias and M. A. Barbosa, *Biomaterials*, 2004, **25**, 4363–4373.
47 T. Kokubo and H. Takadama, *Biomaterials*, 2006, **27**, 2907–2915.